Downloaded from SAE International by RWTH Aachen Univ, Wednesday, December 11, 2024

2022-24-0038 Published 16 Sep 2022

3D-CFD RANS Methodology to Predict Engine-Out Emissions with Gasoline-Like Fuel and Methanol for a DISI Engine

Stefania Esposito, Ali Chaychizadeh, Dominik Golc, Raik Hesse, Joachim Beeckmann, and Heinz Pitsch
RWTH Aachen University

Citation: Esposito, S., Chaychizadeh, A., Golc, D., Hesse, R. et al., "3D-CFD RANS Methodology to Predict Engine-Out Emissions with Gasoline-Like Fuel and Methanol for a DISI Engine," *SAE Int. J. Advances & Curr. Prac. in Mobility* 5(3):1364-1376, 2023, doi:10.4271/2022-24-0038.

This article was presented at the Conference on Sustainable Mobility, September 25-28, 2022.

Received: 25 May 2022 Revised: 04 Jul 2022 Accepted: 19 Jul 2022

Abstract

Renewable fuels, such as bio- and e-fuels, are of great interest for the defossilization of the transport sector. Among these fuels, methanol represents a promising candidate for emission reduction and efficiency increase due to its very high knock resistance and its production pathway as e-fuel. In general, reliable simulation tools are mandatory for evaluating a specific fuel potential and optimizing combustion systems. In this work, a previously presented methodology (Esposito et al., Energies, 2020) has been refined and applied to a different engine and different fuels. Experimental data measured with a single cylinder engine (SCE) are used to validate RANS 3D-CFD simulations of gaseous engine-out emissions. The RANS 3D-CFD model has been used for operation with a toluene reference fuel (TRF) gasoline surrogate and methanol. Varying operating conditions with exhaust gas recirculation (EGR) and air dilution are considered for the two fuels. The laminar flame speed for the fuels has been tabulated by means of detailed chemistry 1D-flame calculations. The G-equation model is used to simulate flame propagation in combination with chemical kinetics to estimate the emission species correctly. The resulting G-equation calibration is compared between the two fuels. Emission results are analyzed, validated with experiments, and compared between the two fuels. The methodology shows a good overall predictivity regarding trends and absolute values. Simulated carbon dioxide (CO_2) shows to be mainly within a 4 % deviation from the measurements. Oxygen (O_2) deviations are within 3 % at lean operation and higher at stoichiometric conditions due to the low overall oxygen content. The maximum nitrogen oxides (NO_x) deviation for the TRF is 22 %, while higher deviations are observed for methanol up to 42.3 %. Total hydrocarbon (THC) emissions are mainly below 20 % deviation. Higher carbon monoxide (CO) deviations are observed due to high CO sensitivity to mixture formation prediction, even if the trends with EGR and air dilution are correctly reproduced. Overall, the methodology shows good potential for virtual pollutant evaluation, assessment of emission reduction strategies, and development of engines with methanol fuel.

Introduction

Simulation models that can predict pollutant emissions from internal combustion engines (ICEs) are crucial for the development of future low-emission propulsion systems. This is especially true for new alternative combustion concepts and fuels. Methanol is one of the most promising alternative fuels for the future of transportation in the perspective of defossilization [1, 2, 3]. Indeed, it can be produced as an e-fuel from renewable energy and, compared to hydrogen, has higher density and overall, fewer challenges connected to safety, fuel tanks, and refueling stations. Additionally, methanol combustion can reach high efficiencies in SI engines due to its high knock resistance and fast laminar burning velocity while simultaneously reducing pollutant emissions. These properties enable increasing the compression ratio and the usage of high dilution levels, which can lead to a strong increase in engine efficiency. For example, Wouters et al. [1] measured an indicated efficiency of 48.7 % with methanol fuel in combination with a compression ratio of 20.6 at very lean operating conditions. This potential of methanol unlocks the possibility of new combustion concepts (e.g., high dilution, high compression ratio, etc.), which need to be developed using reliable simulation tools to optimize their design.

In this context, 3D-CFD Reynolds-averaged Navier-Stokes (RANS) simulations are a widely used tool to optimize new combustion systems [4]. 3D-CFD offers additionally detailed information regarding in-cylinder phenomena, like fuel and residual gas distribution, which impact the pollutant formation mechanisms [5, 6, 7, 8, 9, 10, 11]. However, the correct prediction of gaseous pollutant emissions from spark-ignition (SI) direct injection (DI) engines in 3D-CFD is very challenging as it requires accurate prediction of different physical and chemical aspects simultaneously, primarily mixture formation, flame propagation, and chemical kinetics [12].

Downloaded from SAE International by RWTH Aachen Univ, Wednesday, December 11, 2024

Few studies in literature can be found in which the prediction of gaseous emissions in SI engines has been attempted with 3D-CFD simulations. Duclos [13] et al. simulated and validated only NO_x predictions for a gasoline DI engine at three operating conditions. Kosmadakis et al. [14] evaluated CO, NO, and HC with an SI engine fed with methane/hydrogen mixtures. Other studies [8, 15, 16, 17] present only a numerical investigation of emission trends but without comparison with measurement data. Costa et al. [18] performed gasoline engine RANS simulations for a DI, validated the results of gaseous emissions with experiments, and observed a substantial underestimation of hydrocarbon (HC) emissions. Li et al. [19] simulated a highly stratified DI engine operated with methanol and validated the predictivity regarding NO_x. Overall, only few studies that deal with the validation of RANS 3D-CFD simulation of gaseous emissions from DI SI engines can be found in the literature, especially in combination with methanol.

In this work, a previously developed methodology [12] validated with TRF measurements has been improved and applied to new datasets generated with a different SCE engine and with different fuels (TRF and methanol). In particular, the focus is posed on the verification of the predictivity regarding the emission reduction potential of methanol and emission trends with different kinds of charge dilution.

Methodology

Experimental Setup

The measurement data used to validate the simulation models was obtained with the SI direct injection (DI) research single-cylinder engine (SCE) at ITV of RWTH Aachen University. The DI injector and the spark plug are centrally located in the combustion chamber. The intake ports are symmetrical and designed to achieve a high tumble level. The main data of the engine and the fixed operating conditions used for this study are reported in Table 1.

The engine is coupled with a dynamometer to allow constant speed operation within an accuracy of ±2 min^{-1}. The oil and coolant conditioning systems maintain a constant media temperature of 90 °C. On the intake and the exhaust paths, compensation volumes are installed to dampen pressure oscillations in the peripheries. The fuel mass flow has been measured by the Coriolis principle using an AVL mass flow meter coupled to an AVL fuel conditioning unit. The engine is equipped with a high-pressure exhaust gas recirculation system (EGR) that allows to recirculate exhaust gases from the exhaust system downstream the exhaust compensation volume to the intake side upstream the intake compensation volume. The EGR percentage in the intake manifold is determined by an ECM EGR 5230 dual lambda/O_2 analyzer with an accuracy of ±0.5 % points. The instantaneous absolute pressures in the intake and exhaust are measured via Kistler 4049B piezoresistive transducers. Average temperatures are measured through type-K thermocouples at approximately the same locations. In-cylinder pressure is measured with a Kistler 6056A piezoelectric sensor. The sampling of the exhaust gases to determine the concentration of the gaseous pollutants is performed at a location 130 mm further downstream of the exhaust pressure sensor. The following species concentrations are measured with multiple analyzers: total unburned hydrocarbon (THC) measured as ppm C_3 equivalent (device calibrated with propane), nitrogen oxides (NO_x = NO+NO_2), carbon monoxide (CO) and carbon dioxide (CO_2), and oxygen (O_2). Table 2 summarizes the measurement principles and the devices used for the gaseous emission measurements together with the main device specifications. Figure 1 schematizes the SCE with the key measurement locations. For each operating point, 500 or 1000 cycles have been recorded and used for further analysis.

The experimental uncertainty for the emission measurements is estimated for better evaluation of the emission simulation results. The uncertainty of the measurement devices u is estimated in a simplified way by assuming a rectangular distribution based on the information from the manufacturer with the following formula [20] and the values as stated in Table 2:

$$u = \frac{Linearity \cdot FS}{\sqrt{3}} \tag{1}$$

Operating Points

For this study, measurements performed with a toluene reference fuel (TRF) and with pure methanol are considered. Previous work by the authors showed that a TRF blended using

TABLE 1 SCE main data.

Parameter/variable	Value
Displacement	333 cm^3
Bore / Stroke	71.9 mm / 82.0 mm
Compression ratio	10.5
Intake/exhaust event length (1 mm)	184/185° CA
Fuel injection pressure	20 MPa
Engine speed	2000 min^{-1}

TABLE 2 Gaseous emission measurement devices and their main specifications.

Species	Meas. principle	Analyzer	Range (FS)	Linearity ††	Response time T90 / s
THC	FID*	ABB Fidas 24	0-5000 ppmC_3	2 % FS	<1.5 s
NO_x	CLD‡	ECOPhysics CLD 700	0-10000 ppm	1 % FS	2-32 s
CO	NDIR⁂	ABB Uras26	0-5000 ppm	1 % FS	<2.5 s
CO_2	NDIR⁂	ABB Uras26	0-20 %	1 % FS	<2.5 s
O_2	PMD†	ABB Magnos206	0-25 %	0.5 % FS	≤3.5 s

* Flame-ionization detector
‡ chemiluminescence detector
⁂ non-dispersive infrared adsorption
† para-magnetic detector
†† in absence of specification, the confidence interval of 95 % is assumed [21].

Downloaded from SAE International by RWTH Aachen Univ, Wednesday, December 11, 2024

FIGURE 1 Schematic of SCE with location of the low-pressure indication sensor positions (intake and exhaust) and emission measurement sampling location.

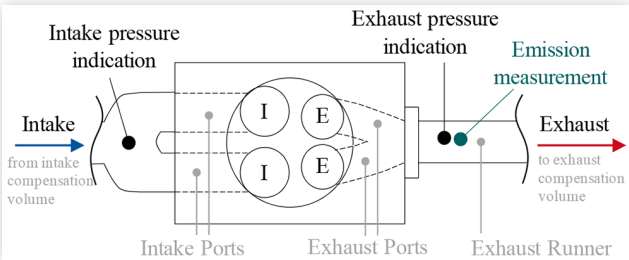

the method of vom Lehn et al. [22] provided global gaseous emission values that match the emission levels of a market gasoline [23]. For this reason, the TRF fuel can be considered as a good representative for gasoline. As in previous studies [12], the focus is on the 3D-CFD prediction capability regarding gaseous emissions. To not introduce additional inaccuracies coming from the fuel modeling, the usage of the exact same fuel between simulation and experiments is preferred. The TRF was formulated in order to perfectly match the octane numbers of a reference RON100 gasoline and, for this reason, has an unusually high toluene content. The TRF composition in mass fractions is 0.849 of toluene, 0.134 of n-heptane, 0.017 of iso-octane.

Similar operating conditions have been selected between the two fuels in order to allow a better comparison regarding the emission reduction potentials with methanol operation. Additionally, operating points with different types of dilution (EGR and air) are investigated in order to check the predictivity of the models under different operating conditions. Table 3 summarizes the selected operating conditions for both fuels considered in this study.

Simulation Setup

Geometry and Meshing The engine geometry between intake and exhaust pressure sensors has been modeled in a CAD software and imported in CONVERGE CFD v3.0. Since the piston top-land crevice is the major contribution to HC emissions [24, 25], its geometry has been included for a more realistic estimation of the HC emissions [12]. A visualization of the simulation domain is provided in Figure 2.

FIGURE 2 Visualization of the simulation domain.

The software provides an automatic meshing based on a defined base mesh grid (δ_B). Some additional mesh embedding in specific zones and for specific periods can be implemented as well as automatic mesh refinements (AMR) based on some specified cell-gradient criteria. The refinements of n degree, both embedding and AMR, result in a cell size δ_n that has a reduced size of $\delta_B/2^n$. The base mesh grid δ_B in this work is selected as 4 mm. Table 4 presents the mesh embedding and the AMR settings used for the simulation.

Boundary and Initial Conditions The pressure and temperature boundary conditions are generated through the post-processing of the measurement data with a three-pressure analysis (TPA) in GT-SUITE [26]. The intake flow consists of fresh air (76.8 % N_2 and 23.2 % O_2 in mass) and for the relevant cases, EGR which is simplified as a mixture of CO_2, H_2O, CO, NO, N_2, and O_2 plus C_3H_8 to account for the mass of HC in the EGR. The exhaust gas composition, both for the EGR and the exhaust boundary condition, is estimated based on the measured gaseous emissions for the selected operating points.

The simulation is started in the second half of the exhaust stroke to avoid simulating the first half of the exhaust stroke, where high flow velocity across the exhaust valves reduces drastically the simulation time-step. The initial pressures and temperatures in the different regions are also obtained from the TPA. The intake region is initialized with fresh air (with or without EGR) while the cylinder and exhaust regions are initialized with the burned gas composition (as the EGR). The so-initialized simulation is carried on for multiple full

TABLE 3 Operating conditions selected for this study.

Fuel	TRF (Gasoline-like, G)			Methanol (M)		
OP* name	G-L1-E0	G-L1-E20	G-L1.4-E0	M-L1-E0	M-L1-E20	M-L1.4-E0
IMEP/bar	**16**	13	13	**16**	13	13
λ† / -	1.0	1.0	**1.4**	1.0	1.0	**1.4**
EGR /%	0	**20**	0	0	**20**	0
Valve overlap / ° CA	25	25	25	30	25	25
SOI‡ /° CA b TDC**	260	260	260	260	270	260

* Operating point, OP names include fuel, air-fuel-ratio, and EGR level.
† relative air-fuel ratio
‡ start of injection
** before top-dead center.

Downloaded from SAE International by RWTH Aachen Univ, Wednesday, December 11, 2024

TABLE 4 Mesh embedding and AMR settings.

Mesh embedding settings				
Area	Period (° CA)			*n*
Cylinder region	permanent			2
Injector spray	SOI+100°			3
Spark plug *r* = 1 mm	[ST-3°, ST+7°]*			4
Spark plug *r* = 3 mm	[ST-3°, ST+7°]*			3
Cylinder gasket	permanent			3
Piston top-land crevice	permanent			3
Intake valve gap	intake valves open			1
Exhaust valve gap	exhaust valves open			1
AMR settings				
Region	AMR variable	Period (° CA aTDC‡)	Criterion	*n*
Cylinder	velocity	permanent	1 m/s	2
Cylinder	temperature	[-120°, +120°]	2.5 K	3
Intake	velocity	intake valves open	1 m/s	2
Exhaust	velocity	exhaust valves open	1 m/s	2

* spark timing
‡ after top dead center.

consecutive cycles in order to achieve steady-state composition in the exhaust path for emission evaluation. The wall temperatures are set in agreement to the temperatures assumed for similar operating conditions in [12].

Models The simulation methodology is based on the previous work by the authors [12]. The major models used in the simulations are summarized in Table 5. For the spray break-up the Kelvin-Helmholtz/Rayleigh-Taylor (KH-RT) hybrid model [27] has been calibrated to match the spray penetration measured with the static injection optical measurements with n-heptane.

Regarding the combustion model, a similar methodology has been used as in [12]. The SAGE chemical kinetic solver [28] available in CONVERGE has been kept active throughout all the simulation time for the cells that exceed 600 K and concentrations of CO+HC above 0.1 ppm. The reduced version of the mechanism from Cai et al. [29] already used and published in [12] has been used for the TRF fuel. It consists of 239 species and 1068 reactions. For the methanol oxidation, the methanol sub-mechanism from the mechanism of Cai et al. [29] has been isolated and consists of 62 species and 425 reactions. Both mechanisms are featured with detailed NO_x mechanism from Lamoureux [30].

TABLE 5 Standard models applied in the simulation.

Physical phenomenon	Model
Turbulence	Standard $k-\varepsilon$
Spray break-up	KH-RT
Film splash	O'Rourke
Velocity and temperature boundary layer	Law of the wall
Wall heat transfer	O'Rourke and Amsden

In order to focus on the emission prediction capability of the model, the combustion profile has been reproduced by means of a calibrated G-equation model [12]. Differently to the previous study [12], SAGE has been kept active not only in the burned and unburned zones, but also on the flame front which is computationally more expensive. This setting is expected to improve the reliability of the emission prediction, especially for NO_x at diluted operation. Another difference to the previously presented methodology regards the laminar flame speed evaluation. Instead of using the model from Gülder [31], 1D laminar flame speed tables have been generated with the available tool in CONVERGE for both fuels, with the mechanism from Cai et al. [29]. The tables consist of a large matrix in terms of pressure (10-130 bar), temperature (500-1800 K), relative air-fuel ratio (0.5-2.5), and EGR percentage (0-40 %). For the TRF, the predictivity of the mechanism regarding the laminar flame speed relies on the original mechanism development which was validated with laminar burning velocity data of mixtures of iso-octane, toluene, n-heptane, and ethanol, as well as multiple other hydrocarbons [29]. A validation of the used mechanism with measurements of laminar burning velocities of methanol-air mixtures is reported in the appendix (Figure A.1).

To highlight the differences between the fuels regarding laminar flame speed, Figure 3 compares varying EGR and λ at the pressure of 2.4 MPa and temperature of 720 K (similar to ignition conditions for the evaluated operating points). It can be observed how methanol shows a higher laminar flame speed at rich and stoichiometric conditions as well as in combination with EGR, while the differences between the two fuels at lean conditions are minor.

As pointed out in [12], there is the necessity to deactivate the G-equation flame propagation model during the last phase of combustion in order to obtain a realistic estimation of the HC emissions. In this work, the same deactivation procedure explained in [12] has been implemented. With this method, the crank angle at which the measured heat release curve shows a significant slowdown is mathematically determined (usually around 90-95 % of fuel mass burned) and used to deactivate the G-equation model. The hypothesis behind this procedure is that the G-equation is necessary to correctly predict the heat release rate only as long as the combustion is

FIGURE 3 Laminar flame speed of TRF and methanol at a pressure of 2.4 MPa and temperature of 720 K.

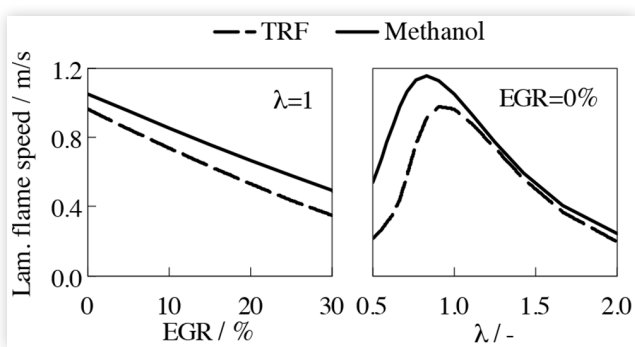

Downloaded from SAE International by RWTH Aachen Univ, Wednesday, December 11, 2024

turbulence-dominated. The last burn-out phase of the combustion with a low heat release rate and low turbulence intensity available is then mainly kinetically controlled and can be accurately predicted only by the SAGE chemical kinetic solver.

The combustion is started by directly initializing the variable G to a positive value in a 0.5 mm sphere between the spark electrodes. In this way, the flame propagation calibration of the G-equation model towards the rest of the combustion chamber (initialized with a negative G value) can start. The calibration of the model has been achieved by optimizing two parameters. Firstly, the spark timing in the simulation (the start of the flame propagation according to the G-equation model) is retarded. Indeed, this simplified ignition procedure does not account for the real complexity of the ignition process and the timing at which the G-equation starts the flame front propagation needs to be retarded compared to the experimental spark timing. Secondly, the b_1 coefficient of the G-equation formula for the turbulent flame speed [32] needs to be calibrated to match the measured heat release rate (standard value from Peters [32] $b_1 = 2.0$).

Emission Evaluation As pointed out in [12], the methodology and the location for pollutant evaluation in 3D-CFD is crucial for correct comparison with measurements. On the basis of multiple studies [12, 23, 33], the authors demonstrated how emission values and trends are different at different sampling locations and how the evaluation in CFD should mimic as much as possible the real emission sampling location to allow a proper comparison with the measured emission values. The best option is to evaluate species concentration at the same location as the emissions were sampled in the measurements as presented in [12]. However, in this work and in contrast to the previous work [12], the emission sampling location is approximately 130 mm further downstream the exhaust pressure transducer; thus, outside the simulation domain. Nevertheless, as shown in [33], the emission trends and values are similar in the exhaust runner and do not change strongly for different locations. Especially for the distances considered in this case, the inaccuracy introduced by the usage of a CFD sampling position of approximately 130 mm further upstream the real sampling position seems to be negligible in comparison to the inaccuracies of the emission measurement devices and of the simulation models. This might not be a valid assumption in cases where the emission measurement devices are applied even further downstream (e.g., longer distances, after the compensation volume, after a turbo-charger, etc.) when emission trends over crank angle, corresponding average values, and time scales for the emission sampling are expected to change significantly. In order to remove the influence of the composition of the gases at the exhaust boundary, the emission sampling location in the simulation is moved approximately 40 mm further upstream of the exhaust boundary (in total 170 mm upstream of the real emission sampling position).

Apart from the location of the emission sampling in the simulation, the evaluation method for gaseous emissions in the exhaust system plays a crucial role. This aspect will be deepened in the results section, where different emission evaluation procedures will be presented and compared. Figure 4 presents a visualization of the emission measuring locations used for the emission evaluation.

FIGURE 4 Sensor locations considered for emission evaluation.

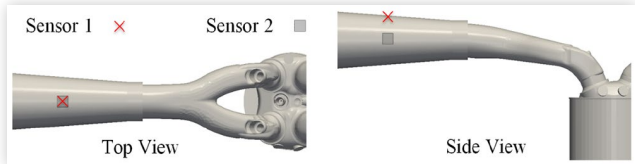

For the evaluation of the HC, a C_3 equivalent THC value is built on the basis of all the available HC species in order to be able to compare the results with the measurements. The conversion of the HC-species concentration to the C_3 equivalent HC is performed with an ideal FID factor, i.e., multiplying by the number of C-atoms of the specific species and dividing by 3. However, as mentioned in [12], the real FID factors can differ from the real ones and this aspect constitutes a source for inaccuracies.

Simulations of multiple consecutive cycles were performed to achieve a cyclically repeatable pattern of concentrations in the exhaust runner. Figure 5 reports the pollutant mole fractions in the exhaust port for the first five simulated cycles for the case G-L1.4-E0. The fifth cycle was the final one that has been considered further in the paper. Overall, it can be observed that after the first three cycles, no significant changes in the pollutant mole fraction patterns are detectable anymore. For all the investigated cases, four to five consecutive cycles have been simulated.

FIGURE 5 Simulated pollutant mole fractions evaluated at sensor 1 (Figure 4) for the first five consecutive cycles for the case G-L1.4-E0.

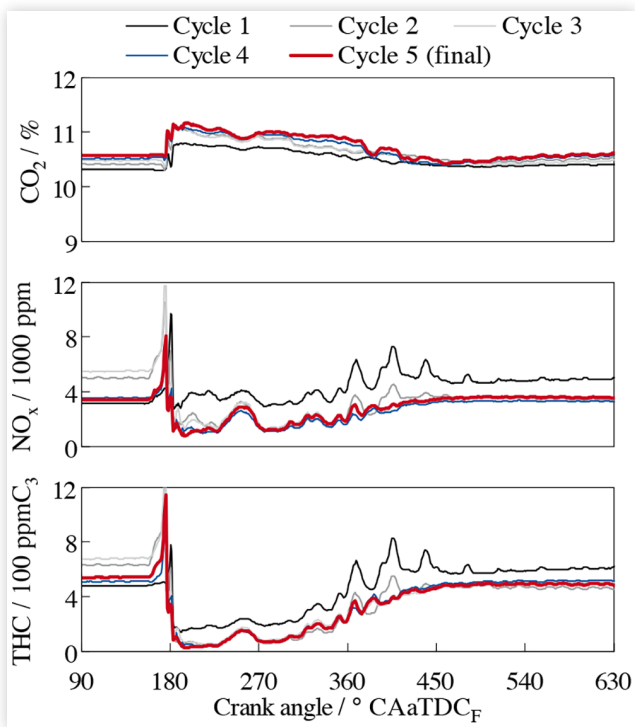

Downloaded from SAE International by RWTH Aachen Univ, Wednesday, December 11, 2024

Results

Combustion Calibration

The results of the G-equation calibration regarding b_1 coefficient and spark timing as well as the G-equation deactivation timing (α_{G0}) and the mass of fuel burned at the G-equation deactivation ($x_{b,\,G0}$) are summarized in Table 6.

First of all, it can be noted that the selected b_1 values are constant for a given fuel and very similar between the two fuels. Additionally, also the spark timing delays (ΔST) to be applied in simulation follow a similar trend over the operating conditions for both fuels. The agreement between the simulated and measured cylinder pressure (p_{cyl}) and heat release rate ($\dot{Q}_{cyl}$) for all the operating points are reported in Figure 6. Even if the combustion profile was calibrated pointwise, it was preferred to have a calibration that is as similar as possible between the fuels and among the operating points. The scope was to highlight the possibility of using the G-equation model without the need for extremely different calibration. With this procedure, a good overall agreement between the simulation and measured pressure is observable. It can be noted that a tendency to underestimate the average pressure trace and the heat release rate is observable in the simulation of the methanol cases, especially at diluted conditions. However, since the underestimation of the peak pressure can influence the pollutant emissions (especially for NO_x), a sensitivity analysis to the combustion calibration will be presented at the end of the result section.

For all the cases, a characteristic shape of the heat release rate is observed with a peak in the first half of the combustion duration. This peak occurs after the contact of the flame with the piston reducing flame area. Similar shapes can be found also in some experimental cycles with similar pressure traces. This characteristic shape is present in all cases because of constant ignition shape and flame propagation mode. Moreover, it can be observed that for all the cases, after the G-equation deactivation, the heat release rate proceeds with a similar trend as in the measurements as already verified in [12]. This is again a confirmation of the validity of the adopted methodology for methanol.

Emission Results

Sensitivity to Engine-Out Emission Evaluation in CFD In this section, different possible evaluations of the species concentrations in CFD are discussed more in detail.

FIGURE 6 Comparison of measured pressure traces and heat release rates (all-cycles and average) and simulation for all the investigated operating points. Timing at which the G-equation model is deactivated is identified with an empty square on the x-axis.

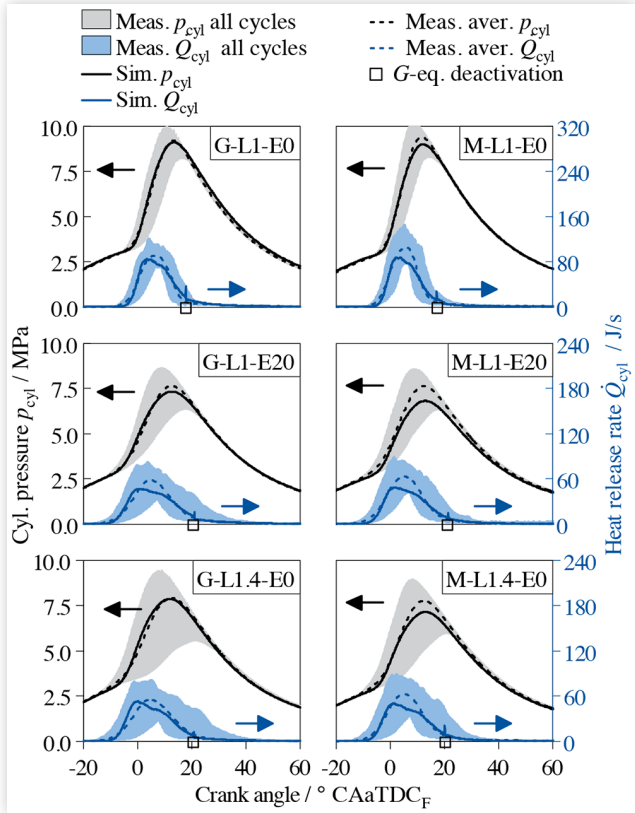

The scope is to point out how varying evaluation methods lead to different values; thus, making this aspect crucial for proper comparison of simulated emission species with measurements. Figure 7 reports multiple plots which are related to possible engine-out emission evaluations in CFD for the case G-L1.4-E0. In particular, Figure 7a shows the trend of total pressure in the exhaust region and the mass flow rate at the exhaust boundary; Figure 7b shows the instantaneous mole fractions for selected species, CO_2 (Figure 7b.1) and HC (Figure 7b.2), evaluated at different locations and compared to the measured value and the corresponding mole fraction in the cylinder at exhaust valve opening (EVO); Figure 7c shows multiple possible and common evaluation methods of the CFD data at different locations and different kinds of averaging (based on time, pressure, and mass flow). In the authors'

TABLE 6 Results of the G-equation methodology and calibration.

Fuel	TRF (Gasoline-like, G)			Methanol (M)		
OP* name	G-L1-E0	G-L1-E20	G-L1.4-E0	M-L1-E0	M-L1-E20	M-L1.4-E0
b_1	2.35			2.40		
ST_{EXP}/°CA aTDC	-12.0	-22.5	-21.0	-12.0	-20.0	-18.0
ΔST/°CA	3.0	3.5	5.5	3.0	4.5	4.0
α_{G_0}/°CA aTDC	17.8	21.0	20.7	17.2	21.3	20.1
$x_{b,\,G0}$ / %	90 %	93 %	95 %	93 %	94 %	93 %

Downloaded from SAE International by RWTH Aachen Univ, Wednesday, December 11, 2024

FIGURE 7 Comparison of different engine-out emission evaluation methods in CFD. OP G-L1.4-E0: (a) exhaust pressure (left) and exhaust mass flow rate (right), (b) instantaneous emission trends for CO_2 (b.1) and THC (b.2), (c) different emission evaluation methods in CFD compared to measured mole fractions for CO_2 (c.1) and THC (c.2).

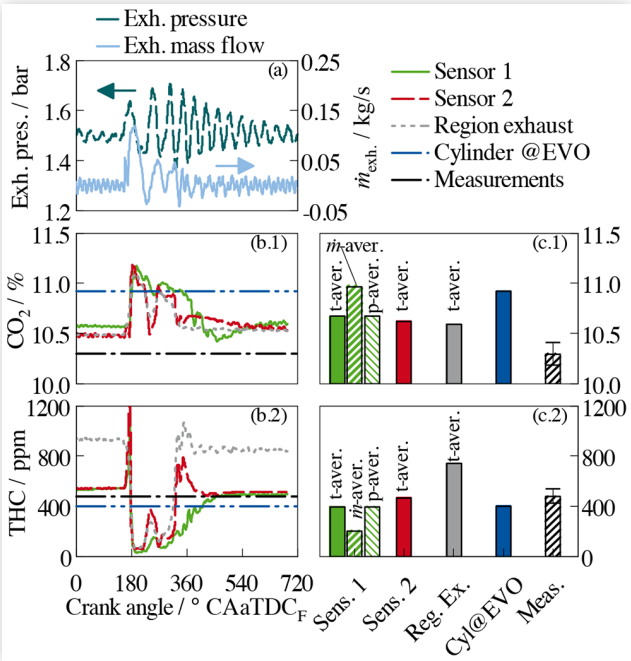

opinion, the most representative value to be compared with the experimental results is a time-averaged mole fraction at the emission sampling location, which in this case is approximated by sensor 1 (see Figure 4). Indeed, the emission measurement devices are sampling continuously exhaust gases due to their near-vacuum inner pressure. Additionally, they are connected through multiple meter-long pipes to the analyzers where mixing can occur. Moreover, the response time of the devices is longer than the engine cycles. According to all the aforementioned reasons and on the basis of the results from previous studies [23, 33], the measurement value seems better represented by a time average of the mole fraction of specific species at the measurement location.

For emitted species that do not show a highly dynamic trend over crank angle as CO_2, different evaluations of the species concentration in CFD lead to negligible differences in the range of few percent (note the quite enlarged scale for the CO_2 plots). On the other hand, the HC concentrations show always a highly dynamic trend over crank angle because of the top-land crevice mechanism [12, 33]. In this case, different evaluations lead to very different values which can differ from each other by more than 50 %. In particular, an intuitively suitable evaluation like the mass-flow averaging of the mole fraction value at the sensor location (see Figure 7c.2) seem to be quite inaccurate for the HC evaluation because of the very low value of HC during the exhaust phase (when the mass flow is not 0).

For all these considerations, only the time-averaged values at the location of sensor 1 will be considered further in this work for the comparison with measurement values.

Engine-Out Emission Validation

Figure 8 reports the comparison of emissions evaluated in CFD with the measured emitted species (CO_2, O_2, CO, NO_x, THC). Overall, it can be observed that the simulated emission values follow the trend and the absolute values of the measurements quite accurately. Table 7 reports the measurement uncertainty converted in ± % for each operating point, while Table 8 reports the relative deviation in % of all the simulated emission values with respect to the corresponding measurements. It can be noted that the deviations in CO_2 emissions are mainly below 4 % for both fuels, while only at lean condition with methanol this deviation reaches up to 7.5 %. This can result from a higher inaccuracy in the prediction of the fuel oxidation, which seems to be more complete in the simulation of the lean case. This hypothesis is confirmed by the underestimation of CO, THC, and O_2 for the lean case. Regarding O_2 emissions, high relative deviations are observed in almost all the points at stoichiometric conditions because of the low overall O_2 level (below 1 %vol.). In this case, slight inaccuracies in the air-fuel ratio can be the cause for these deviations. For the lean cases, the O_2 shows a maximum deviation below 3 %. As far as CO is concerned, a strong overestimation at stoichiometric conditions is observed for both fuels, strongest for the methanol cases. This is in line with the previous study from the authors [12] and it is probably due to inaccuracies in the mixture formation and the injection modeling. It has to be noted at this point that the injector penetration has been

FIGURE 8 Validation of simulated engine-out emissions with measurements and comparison between the two fuels.

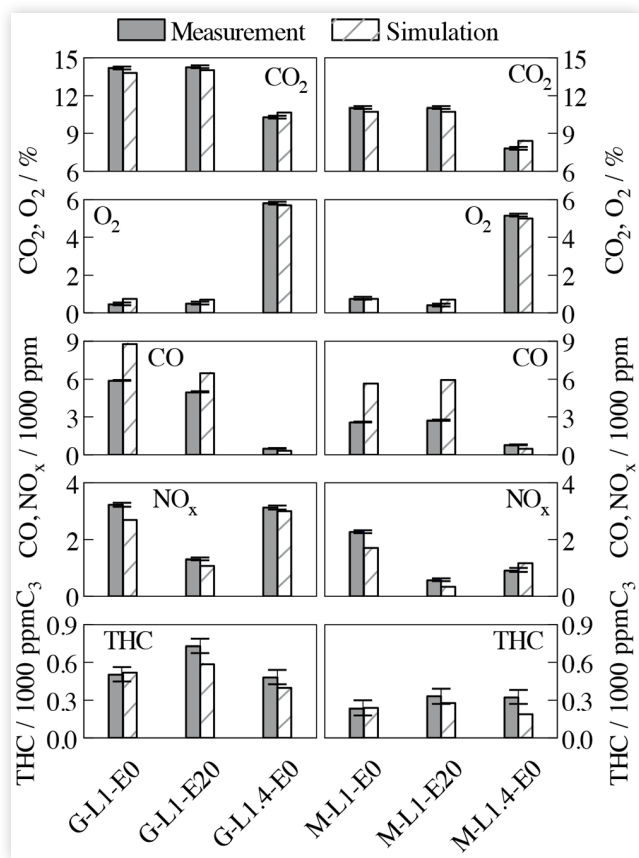

Downloaded from SAE International by RWTH Aachen Univ, Wednesday, December 11, 2024

TABLE 7 Measurement uncertainty quantified relatively to the measurement value in %. Operating points with uncertainties higher than 10 % of the measured values are marked in bold.

Uncertainty / ±%	G-L1-E0	G-L1-E20	G-L1.4-E0	M-L1-E0	M-L1-E20	M-L1.4-E0
CO_2	0.8	0.8	1.1	1.0	1.0	1.5
O_2	**15.8**	**14.6**	1.2	9.8	**18.1**	1.4
CO	0.5	0.6	6.2	1.1	1.1	3.8
NO_x	1.8	4.4	1.8	2.6	**10.3**	6.3
THC	**11.5**	7.9	**12.1**	**24.5**	**17.6**	**18.0**

TABLE 8 Relative deviation of simulated emission values to measured values. Values higher than the measurement uncertainty are marked as bold and a color scale highlights the magnitude of the deviation: green for deviation within 5 % (or values within the experimental uncertainty), light green for values within 5-25 %, orange for deviations within 25-50 %, red for deviations above 50 %.

Rel. deviation / %	G-L1-E0	G-L1-E20	G-L1.4-E0	M-L1-E0	M-L1-E20	M-L1.4-E0
CO_2	**-2.9**	**-1.5**	**+3.7**	**-3.2**	**-2.8**	**+7.5**
O_2	**+68.5**	**+41.6**	**-2.1**	**+1.2**	**+72.0**	**-2.9**
CO	**+50.7**	**+30.8**	**-34.6**	**+121.4**	**+120.0**	**-39.8**
NO_x	**-16.5**	**-19.1**	**-4.2**	**-24.9**	**-42.3**	**+26.8**
THC	+3.2	**-19.5**	**-16.9**	+0.4	-15.3	**-41.9**

calibrated with available optical injector measurements in a constant volume pressure chamber with n-heptane. Since n-heptane is more similar to the TRF fuel than to methanol, a possible hypothesis is that the higher deviation in CO emissions for the methanol cases result from higher inaccuracies of the current injector model calibration with this fuel.

Considering NO_x emissions, better accuracy is observed for the gasoline-like fuel with a maximum deviation of 22 %. For methanol, higher deviations are calculated, up to 42.3 %. This result is definitely influenced by the lower predicted peak pressure (see Figure 6) compared to the average cylinder pressure in the measurements. Additionally, this phenomenon could be connected to the chemical kinetic mechanism and the interaction of the base chemistry with the NO_x mechanism. Finally, regarding THC emissions, a good predictivity of the model can be observed with deviations from the measurements mainly below 20 %, which is an outstandingly good value for these species despite their complex formation mechanisms. Overall, a tendency towards an underestimation of THC emissions with charge dilution (both EGR and lambda) can be observed for both fuels. This tendency might result from the increased flame and oxidation quenching with diluted charge, which is not accounted practically in the simulation because of the mesh size, which is larger than the quenching distances. This statement seems to be particularly true with methanol operation at lean condition. For this operating point, also the measured value shows a different trend compared to the gasoline-like fuel. Indeed, the measured THC value with no dilution is higher than the lean case for the gasoline-like fuel, but lower for methanol. This observation can lead to the conclusion that the flame quenching for methanol can have a stronger impact on the HC emissions than for the gasoline-like fuel leading to a stronger deviation in simulation.

To visualize emission species mechanisms and distribution in the combustion chamber, 2D sections are shown in Figure 9 for the cases G-L1-E0 and M-L1-E0. In particular, distributions of lambda, temperature, NO_x, CO, and THC are

FIGURE 9 Contour plots of multiple in-cylinder quantities for the cases G-L1-E0 and M-L1-E0: (from left to right) lambda, temperature, NO_x, CO, and THC.

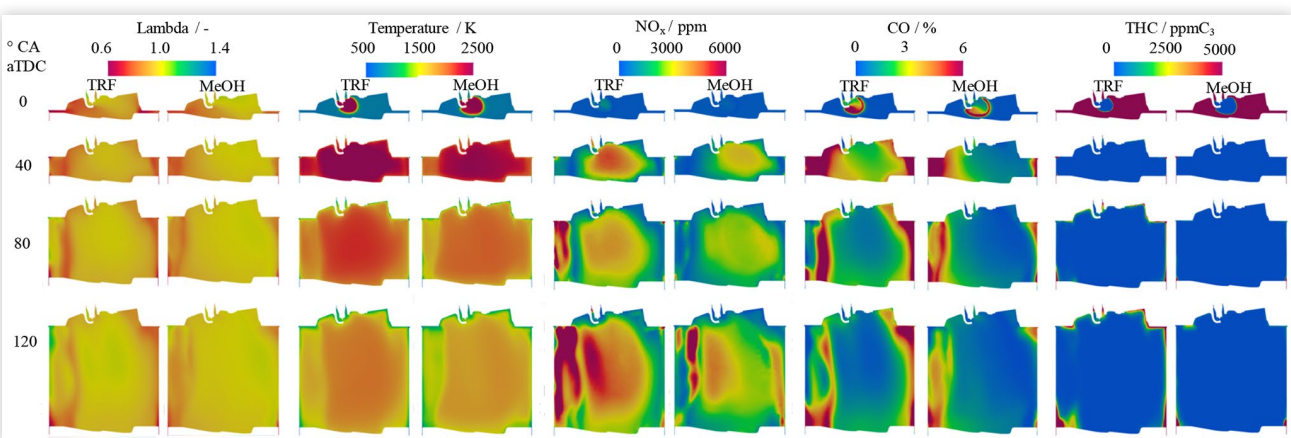

Downloaded from SAE International by RWTH Aachen Univ, Wednesday, December 11, 2024

presented on a section passing through the middle of the combustion chamber between both the intake (on the right side of the section) and the exhaust valves (on the left side of the section) at different crank angles in the expansion stroke (0°, 40°, 80°, 120° CAaTDC). Figure 10 shows multiple quantities evaluated in the cylinder region for the cases G-L1-E0 and M-L1-E0. As far as lambda is concerned, similar distributions can be observed for both fuels even though richer zones are reduced for methanol operation. The peak temperature in the methanol case is also lower due to lower end-compression temperature resulting from higher evaporation enthalpy of methanol. Strongly reduced NO_x production is observable in the methanol case in both Figure 9 and Figure 10, while for both fuels a high NO_x mole fraction is observable on the left side of the contour plots of Figure 9 because of a swirl motion that brings NO_x to the selected section. Also, lower CO production is observable for the methanol case, even if similar CO production near the walls is observable for both fuels due to lower temperature of the mixture and heat transfer to the walls. As far as THC is concerned, higher amounts of THC near the walls are visible for the TRF fuel compared to methanol. Similar plots to Figure 10 for the other operating points are reported in the appendix for completeness (Figure A.2 and Figure A.3).

Additionally, in Figure 11, simulated values of other pollutants of interest like methane (CH_4) and formaldehyde (CH_2O) are compared between the two fuels. In particular, methane is interesting because of its global warming potential (28-34 times higher than CO_2 [34]), while formaldehyde is relevant because of its toxicity [35].

FIGURE 10 Quantities in the cylinder region for the cases G-L1-E0 and M-L1-E0: pressure, temperature, CO_2, CO, NO_x, and THC.

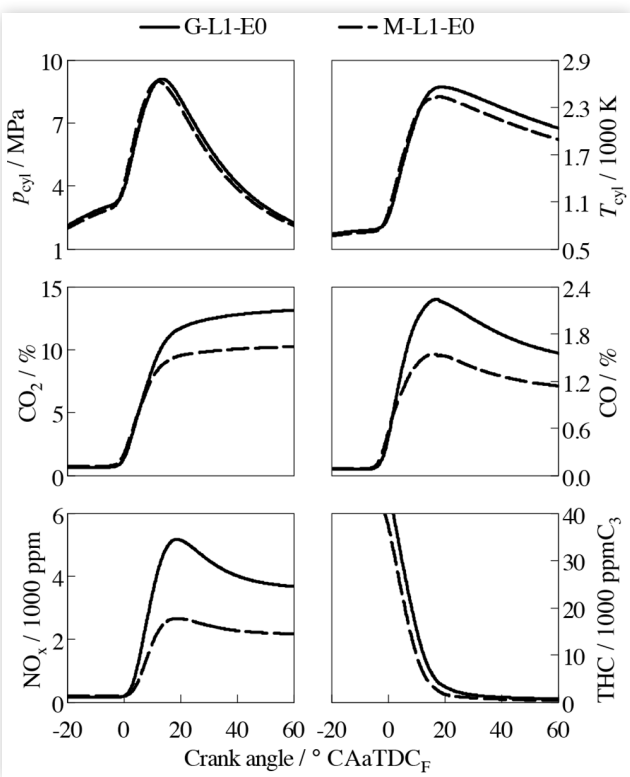

FIGURE 11 Comparison of simulated CH_4 and CH_2O emissions for the two fuels and all the investigated operating conditions.

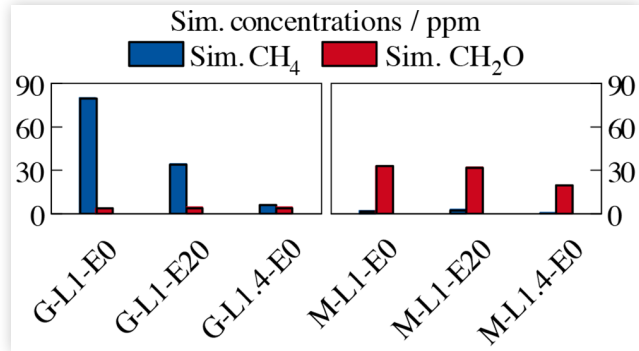

It can be observed that the gasoline-like fuel leads to significant methane emissions, which are absent in the exhaust in case of methanol fueling. On the other side, formaldehyde emissions, which are practically absent in the exhaust of gasoline-like fuels, are detectable in the exhaust of the methanol cases.

Sensitivity to Combustion Calibration As mentioned in the combustion calibration section, similar calibration between both fuels and among the operating conditions has been preferred to highlight the prediction capability of the G-equation model. However, since an underestimation of NO_x has been observed for the cases in which the peak pressure is underestimated, a sensitivity analysis to the combustion calibration is reported in the following for the case M-L1-E20 where the mismatch between the average measured pressure trace and the simulated pressure is the largest. An alternative calibration of the combustion for that operating point has been attempted with the scope of matching better the peak pressure. The improved alternative calibration results in a b_1 of 3.2 and a delay in spark timing of 8° CA. Figure 12 reports the in-cylinder values of pressure, temperature, CO_2, CO, NO_x, and THC concentrations for the base calibration (Table 6) together with the same quantities for the improved calibration. It can be observed that the improved calibration achieves better agreement in the peak pressure and results in a difference in peak temperature of about 60 K, as well as faster CO_2 production and fuel/THC consumption. However, as expected, only for NO_x, the end value in the expansion stroke changes significantly, with an increase of approximately 18 %. It must be noted that the NO_x concentration before the start of combustion is influenced by the previous cycle (in this case, in both simulations performed with the base calibration of Table 6). For this reason, it can be expected that even a higher increase in NO_x than 18 % is possible by simulating multiple cycles with the improved calibration. However, the magnitude of the improvement through the improved combustion calibration does not completely fill the gap of -42.3 % (Table 8) between the simulated and measured values. Thus, other sources of inaccuracy like mixture formation or kinetic mechanism can possibly contribute further to this deviation.

Downloaded from SAE International by RWTH Aachen Univ, Wednesday, December 11, 2024

FIGURE 12 Quantities in the cylinder region for the case M-L1-E20 with the base combustion calibration and the improved calibration: pressure, temperature, CO_2, CO, NO_x, and THC.

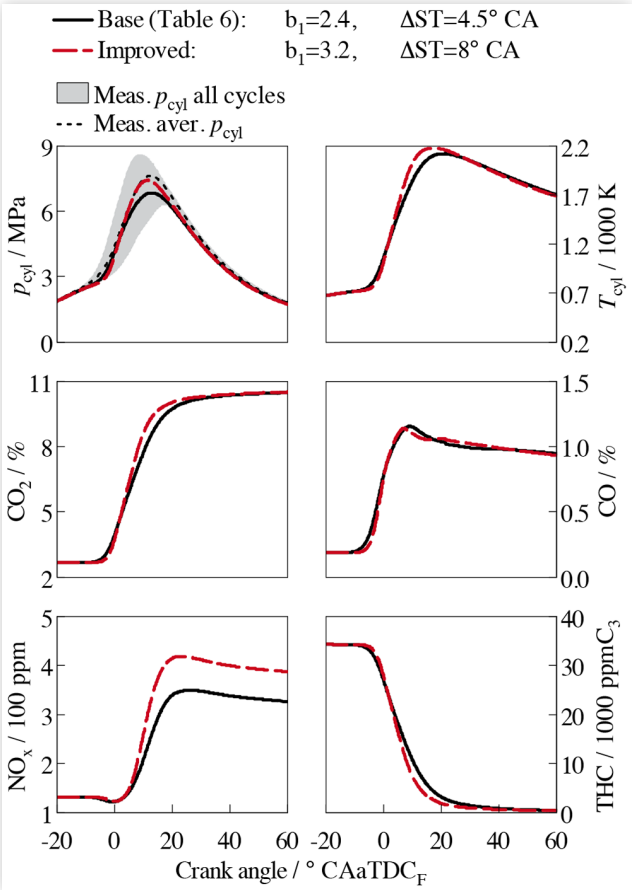

Summary and Conclusion

In this study, a simulation methodology for predictions of gaseous engine-out emissions has been further developed and validated with measurements from an SCE research engine using methanol and a gasoline-like fuel. A calibrated G-equation model has been used to reproduce the pressure profile and evaluate the methodology's predictivity regarding gaseous engine-out emission. The G-equation model calibration showed constant b_1 coefficient for the same fuel and a relatively constant spark delay compared to the measurements. This study showed that the G-equation model could also be used with a reasonable prediction capability for further operating points of the same engine by assuming similar calibration parameters. The modified methodology improved emission predictivity for CO_2, O_2, CO, THC, and NO_x compared to the previous study [12] for a TRF gasoline surrogate. Higher CO, HC, and NO_x deviations are observable in the methanol simulation. These can be attributed to multiple aspects like the kinetic mechanisms involved, increased flame quenching phenomena, and higher inaccuracies in the injection modeling. Overall, the methodology showed the capability to predict emission trends and values at different operating conditions and the emission reduction potential by adopting methanol as fuel compared to a gasoline-like fuel. Indeed, the simulation correctly predicted the lower CO_2, CO, NO_x, and HC emissions from methanol operation.

Moreover, this work presents a unique focus on different methods of emission evaluation in CFD and a rigorous validation of the simulation results with the inclusion of the measurement uncertainties. The proposed emission measurement methodology is the result of multiple experimental and numerical works on gaseous emission evaluation and represents a guideline for future numerical studies in this field.

Future work will be focused on the further development of the simulation methodology to improve the predictivity of the model. Aspects to be investigated include the influence of injection model calibration, kinetic mechanism for NO_x prediction, and flame quenching behavior at diluted operating conditions.

Acknowledgments

The authors thank FORD Werke GmbH for providing the research engine used for this study. The authors are also thankful to Convergent Science Inc. for providing licenses for CONVERGE CFD.

Contact Information

Stefania Esposito
Institute for Combustion Technology
RWTH Aachen University
Templergraben 64, 52056 Aachen
Tel: +49 241 80 94877
Fax: +49 241 80 92923
s.esposito@itv.rwth-aachen.de
www.itv.rwth-aachen.de

References

1. Wouters, C., Burkardt, P., and Pischinger, S., "Limits of Compression Ratio in Spark-Ignition Combustion with Methanol," *International Journal of Engine Research* 23, no. 5 (2022): 793-803, doi:10.1177/14680874211043390.
2. Kalghatgi, G., Agarwal, A.K., Leach, F., and Senecal, K., *Engines and Fuels for Future Transport* (Singapore: Springer Singapore, 2022), ISBN:978-981-16-8716-7.
3. Verkehrwende A., "The Future Cost of Electricity-Based Synthetic Fuels," 2018.
4. Morcinkowski, B., Adomeit, P., Mally, M., Esposito, S. et al., "Emissionsvorhersage in der Entwicklung ottomotorischer EU7-Antriebe," in: , *Experten-Forum Powertrain: Ladungswechsel und Emissionierung 2019*, (2020).
5. Addepalli, S.K., Saw, O.P., and Mallikarjuna, J.M., "Effect of Mixture Distribution on Combustion and Emission Characteristics in a GDI Engine - A CFD Analysis," SAE Technical Paper 2017-24-0036, 2017, https://doi.org/10.4271/2017-24-0036.

Downloaded from SAE International by RWTH Aachen Univ, Wednesday, December 11, 2024

6. Cao, L., Su, H., Mosbach, S., Kraft, M. et al., "Studying the Influence of Direct Injection on PCCI Combustion and Emissions at Engine Idle Condition Using Two Dimensional CFD and Stochastic Reactor Model," SAE Technical Paper 2008-01-0021, 2008, https://doi.org/10.4271/2008-01-0021.
7. Coskun, G., Soyhan, H.S., Demir, U., Turkcan, A. et al., "Influences of Second Injection Variations on Combustion and Emissions of an HCCI-DI Engine: Experiments and CFD Modelling," *Fuel* 136 (2014): 287-294, doi:10.1016/j.fuel.2014.07.042.
8. Jadhav, P.D. and Mallikarjuna, J.M., "Effect of EGR on Performance and Emission Characteristics of a GDI Engine - A CFD Study," SAE Technical Paper 2017-24-0033, 2017, https://doi.org/10.4271/2017-24-0033.
9. Jiao, Q. and Reitz, R.D., "Modeling of Equivalence Ratio Effects on Particulate Formation in a Spark-Ignition Engine under Premixed Conditions," SAE Technical Paper 2014-01-1607, 2014, https://doi.org/10.4271/2014-01-1607.
10. Jiao, Q. and Reitz, R.D., "The Effect of Operating Parameters on Soot Emissions in GDI Engines," *SAE Int. J. Engines* 8, no. 3 (2015): 1322-1333, doi:10.4271/2015-01-1071.
11. Distaso, E., Amirante, R., Tamburrano, P., and Reitz, R.D., "Understanding the Role of Soot Oxidation in Gasoline Combustion: A Numerical Study on the Effects of Oxygen Enrichment on Particulate Mass and Number Emissions in a Spark-Ignition Engine," *Energy Conversion and Management* 184 (2019): 24-39, doi:10.1016/j.enconman.2019.01.022.
12. Esposito, S., Mally, M., Cai, L., Pitsch, H. et al., "Validation of a RANS 3D-CFD Gaseous Emission Model with Space-, Species-, and Cycle-Resolved Measurements from an SI DI Engine," *Energies* 13, no. 17 (2020): 4287, doi:10.3390/en13174287.
13. Duclos, J.P., Zolver, M., and Baritaud, T., "3D Modeling of Combustion for DI-SI Engines," *Oil & Gas Science and Technology - Revue d'IFP Energies Nouvelles* 54, no. 2 (1999): 259-264, doi:10.2516/ogst:1999023.
14. Kosmadakis, G.M., Rakopoulos, D.C., and Rakopoulos, C.D., "Methane/Hydrogen Fueling a Spark-Ignition Engine for Studying NO, CO and HC Emissions with a Research CFD Code," *Fuel* 185 (2016): 903-915, doi:10.1016/j.fuel.2016.08.040.
15. Reddy, A.A. and Mallikarjuna, J.M., "Parametric Study on a Gasoline Direct Injection Engine - A CFD Analysis," SAE Technical Paper 2017-26-0039, 2017, https://doi.org/10.4271/2017-26-0039.
16. Liu, J., Szybist, J., and Dumitrescu, C., "Choice of Tuning Parameters on 3D IC Engine Simulations Using G-Equation," SAE Technical Paper 2018-01-0183, 2018, https://doi.org/10.4271/2018-01-0183.
17. Rahimi Boldaji, M., Sofianopoulos, A., Mamalis, S., and Lawler, B., "A CFD Investigation of the Effects of Fuel Split Fraction on Advanced Low Temperature Combustion: Comparing a Primary Reference Fuel Blend and Ethanol," *Front. Mech. Eng.* 4 (2018), doi:10.3389/fmech.2018.00006.
18. Costa, M., Marchitto, L., Merola, S.S., and Sorge, U., "Study of Mixture Formation and Early Flame Development in a Research GDI (Gasoline Direct Injection) Engine through Numerical Simulation and UV-Digital Imaging," *Energy* 77 (2014): 88-96, doi:10.1016/j.energy.2014.04.114.
19. Li, Y., Bai, X.-S., Tunér, M., Im, H.G. et al., "Investigation on a High-Stratified Direct Injection Spark Ignition (DISI) Engine Fueled with Methanol under a High Compression Ratio," *Applied Thermal Engineering* 148 (2019): 352-362, doi:10.1016/j.applthermaleng.2018.11.065.
20. Möhrke, P. and Runge, B.-U., *Arbeiten mit Messdaten* (Berlin, Heidelberg: Springer Berlin Heidelberg, 2020), ISBN:978-3-662-60659-9.
21. Gainey, B., Longtin, J.P., and Lawler, B., "A Guide to Uncertainty Quantification for Experimental Engine Research and Heat Release Analysis," *SAE Int. J. Engines* 12, no. 5 (2019): 509-523, doi:10.4271/03-12-05-0033.
22. Vom Lehn, F., Cai, L., and Pitsch, H., "Sensitivity Analysis, Uncertainty Quantification, and Optimization for Thermochemical Properties in Chemical Kinetic Combustion Models," *Proceedings of the Combustion Institute* 37, no. 1 (2019): 771-779, doi:10.1016/j.proci.2018.06.188.
23. Esposito, S., Cai, L., Günther, M., Pitsch, H. et al., "Experimental Comparison of Combustion and Emission Characteristics between a Market Gasoline and Its Surrogate," *Combustion and Flame* 214 (2020): 306-322, doi:10.1016/j.combustflame.2019.12.025.
24. Esposito, S., Diekhoff, L., and Pischinger, S., "Prediction of Gaseous Pollutant Emissions from a Spark-Ignition Direct-Injection Engine with Gas-Exchange Simulation," *International Journal of Engine Research* (2021): 146808742110050, doi:10.1177/14680874211005053.
25. Esposito, S., Diekhoff, L., Pitsch, H., and Pischinger, S., "Development of Phenomenological Models for Engine-Out Hydrocarbon Emissions from an SI DI Engine within a 0D Two-Zone Combustion Chamber Description," SAE Technical Paper 2021-24-0008, 2021, https://doi.org/10.4271/2021-24-0008.
26. Gamma Technologies, "GT-SUITE 2018: Engine Performance Application Manual," 2018.
27. Reitz, R.D. and Beale, J.C., "Modeling Spray Atomization with the Kelvin-Helmholtz/Rayleigh-Taylor Hybrid Model," *Atomization and Sprays* 9, no. 6 (1999): 623-650, doi:10.1615/AtomizSpr.v9.i6.40.
28. Senecal, P.K., Pomraning, E., Richards, K.J., Briggs, T.E. et al., "Multi-Dimensional Modeling of Direct-Injection Diesel Spray Liquid Length and Flame Lift-off Length using CFD and Parallel Detailed Chemistry," SAE Technical Paper 2003-01-1043, 2003, https://doi.org/10.4271/2003-01-1043.
29. Cai, L., Ramalingam, A., Minwegen, H., Heufer, A.K. et al., "Impact of Exhaust Gas Recirculation on Ignition Delay Times of Gasoline Fuel: An Experimental and Modeling Study," *Proceedings of the Combustion Institute* 37, no. 1 (2019): 639-647, doi:10.1016/j.proci.2018.05.032.
30. Lamoureux, N., Desgroux, P., El Bakali, A., and Pauwels, J.F., "Experimental and Numerical Study of the Role of NCN in Prompt-NO Formation in Low-Pressure CH4-O2-N2 and C2H2-O2-N2 Flames," *Combustion and Flame* 157, no. 10 (2010): 1929-1941, doi:10.1016/j.combustflame.2010.03.013.
31. Gülder, Ö.L., "Correlations of Laminar Combustion Data for Alternative S.I. Engine Fuels," SAE Technical Paper 841000, 1984, https://doi.org/10.4271/841000.

Downloaded from SAE International by RWTH Aachen Univ, Wednesday, December 11, 2024

32. Peters, N., *Turbulent Combustion: Cambridge Monographs on Mechanics* (Cambridge England, New York: Cambridge University Press, 2000), ISBN:0521660823.
33. Esposito, S., Mauermann, P., Lehrheuer, B., Günther, M. et al., "Effect of Engine Operating Parameters on Space- and Species-Resolved Measurements of Engine-Out Emissions from a Single-Cylinder Spark Ignition Engine," SAE Technical Paper 2019-01-0745, 2019, https://doi.org/10.4271/2019-01-0745.
34. UNECE, "Methane Management," accessed May 13, 2022, https://unece.org/challenge#:~:text=Methane%20is%20a%20powerful%20greenhouses,are%20due%20to%20human%20activities.
35. Dai, P., Ge, Y., Lin, Y., Su, S. et al., "Investigation on Characteristics of Exhaust and Evaporative Emissions from Passenger Cars Fueled with Gasoline/Methanol Blends," *Fuel* 113 (2013): 10-16, doi:10.1016/j.fuel.2013.05.038.
36. Jacobs, S., Döntgen, M., Alquaity, A.B.S., Hesse, R. et al., "A Comprehensive Experimental and Kinetic Modeling Study of the Combustion Chemistry of Diethoxymethane," *Energy Fuels* 35, no. 19 (2021): 16086-16100, doi:10.1021/acs.energyfuels.1c01988.
37. Kelley, A.P., Bechtold, J.K., and Law, C.K., "Premixed Flame Propagation in a Confining Vessel with Weak Pressure Rise," *J. Fluid Mech.* 691 (2012): 26-51, doi:10.1017/jfm.2011.439.

Appendix

Mechanism Validation with Methanol Laminar Burning Velocity

The validity of the mechanism to predict laminar burning velocity for methanol-air flames has been checked by comparing the mechanism prediction with measurements performed according to the methodology described in detail by Jacobs et al. [36] in the Supplementary Material. A summary of the experiment is given below.

Laminar flame speed (S_L) experiments of methanol/air flames were measured in a closed spherical combustion chamber using an optical high-speed Schlieren arrangement (recording rate: 25000 frame per second; image magnification 10 pixel/mm). Measurement conditions comprise varying pressures and fuel-air equivalence ratios ($\boldsymbol{\Phi} = \boldsymbol{\lambda}^{-1}$) ranging from 1 atm to 5 bar, and $\boldsymbol{\Phi}$= 0.8 to 1.3, respectively. The unburned mixture's temperature is 423 K. The oxidizer is compressed, dehumidified air with volume fractions of 20.94 % oxygen, 78.13 % nitrogen, and 0.93 % argon. Methanol's purity is > 99 %. Fuel/air mixtures are prepared in a separate premixing vessel using the partial-pressure method and high-accuracy temperature-compensated pressure transducers of type Keller X HTC. Mixture- and initial condition-related uncertainties are estimated to be 3 % of the laminar flame speed. The premixed methanol/air mixtures are centrally ignited via a high-voltage ignition system. The radii of the spherically expanding flames are extracted from the high-speed recordings by measuring the flame's cross-section area. The time derivate of the flame radius represents the local flame propagation speed, which needs to be extrapolated by approaching an unstretched infinite flame radius. Appropriate extrapolation methods are described by Kelley et al. [37]. The unstretched value is converted to unburned gas conditions to obtain S_L using the burned/unburned density ratio determined using thermodynamic data and an equilibrium solver. In Figure A.1, the experimental results for S_L and their error estimates are compared to the 1D planar stationary flame simulations using the chemical kinetic model by Cai et al. [29]. The kinetic model's agreement is within the 95 % confidence interval of the experimental uncertainty limits for all the investigated conditions.

FIGURE A.1 Comparison of laminar flame speed (S_L) data between experiments (symbols) and simulation with Cai et al. [29] mechanism at different pressures and the unburned temperature of 423 K.

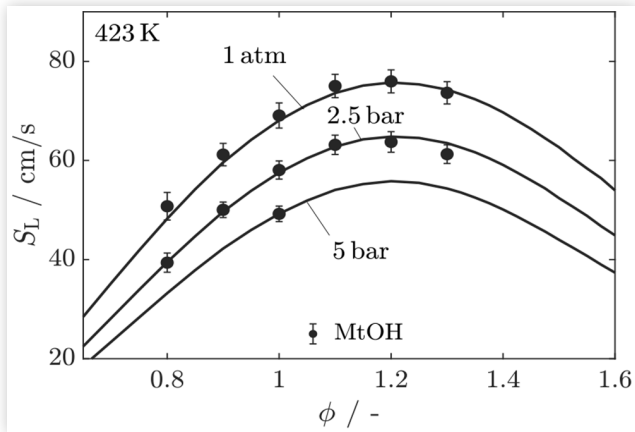

Downloaded from SAE International by RWTH Aachen Univ, Wednesday, December 11, 2024

Further Comparison between TRF and Methanol

FIGURE A.2 Quantities in the cylinder region for the cases G-L1-E20 and M-L1-E20: pressure, temperature, CO_2, CO, NO_x, and THC.

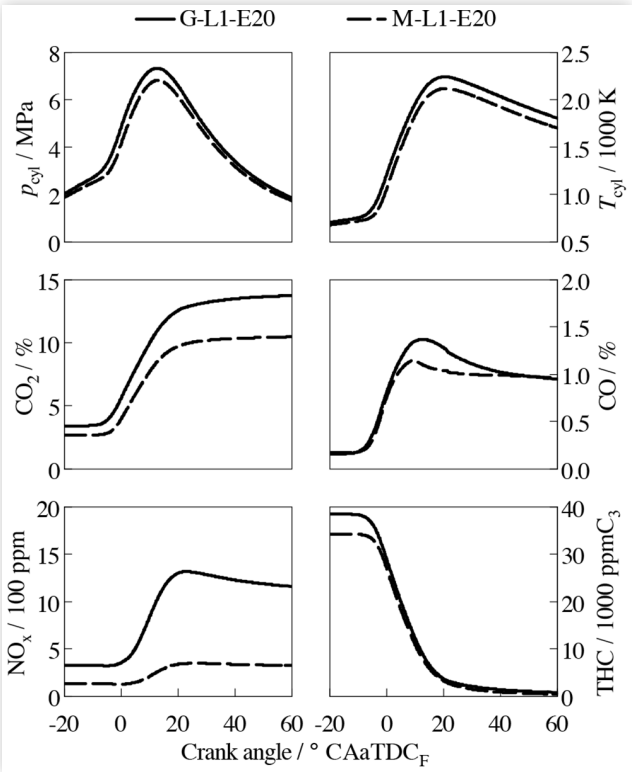

FIGURE A.3 Quantities in the cylinder region for the cases G-L1.4-E0 and M-L1.4-E0: pressure, temperature, CO_2, CO, NO_x, and THC.

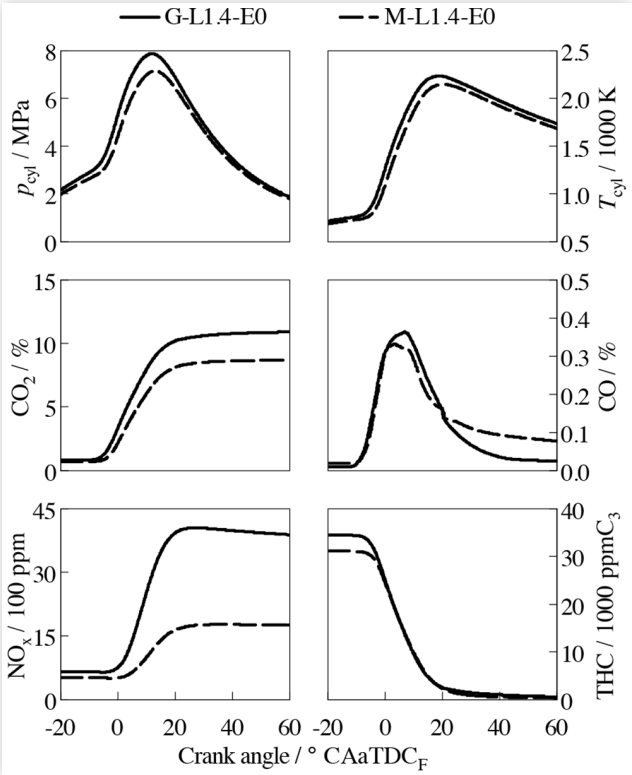

© 2022 SAE International and SAE Naples Section. All rights reserved. No part of this publication may be reproduced, stored in a retrieval system, or transmitted, in any form or by any means, electronic, mechanical, photocopying, recording, or otherwise, without the prior written permission of SAE International.

Positions and opinions advanced in this work are those of the author(s) and not necessarily those of SAE International. Responsibility for the content of the work lies solely with the author(s).

e-ISSN 2641-9645